Asymmetric Impacts of El Niño and La Niña on the Pacific–South America Teleconnection Pattern

YA WANG,[a,b] GANG HUANG,[a,b,c] KAIMING HU,[a,d] WEICHEN TAO,[a] XICHEN LI,[e] HAINAN GONG,[d] LETIAN GU,[b] AND WENQI ZHANG[b]

[a] *State Key Laboratory of Numerical Modeling for Atmospheric Sciences and Geophysical Fluid Dynamics, Institute of Atmospheric Physics, Chinese Academy of Sciences, Beijing, China*
[b] *College of Earth and Planetary Sciences, University of Chinese Academy of Sciences, Beijing, China*
[c] *Laboratory for Regional Oceanography and Numerical Modeling, Qingdao National Laboratory for Marine Science and Technology, Qingdao, China*
[d] *Center for Monsoon System Research, Institute of Atmospheric Physics, Chinese Academy of Sciences, Beijing, China*
[e] *International Center for Climate and Environment Sciences, Institute of Atmospheric Physics, Chinese Academy of Sciences, Beijing, China*

(Manuscript received 13 April 2021, in final form 3 December 2021)

ABSTRACT: El Niño–Southern Oscillation (ENSO) has a huge influence on Antarctic climate variability via Rossby wave trains. In this study, the asymmetry of the ENSO teleconnection in the Southern Hemisphere, together with the mechanisms involved, is systematically investigated. In four reanalysis datasets, the composite atmospheric circulation anomaly in austral winter over the Amundsen Sea during La Niña is situated more to the west than during El Niño. This asymmetric feature is reproduced by ECHAM5.3.2 forced with both composite and idealized symmetric sea surface temperature anomalies. Utilizing a linear baroclinic model, we find that ENSO-triggered circulation anomalies in the subtropics can readily extract kinetic energy from the climatological mean flow and develop efficiently at the exit of the subtropical jet stream (STJ). The discrepancy in the location of the STJ between El Niño and La Niña causes asymmetric circulation responses by affecting the energy conversion. During El Niño years, anomalous tropical convective precipitation increases the meridional temperature gradient, which in turn leads to the strengthening of the STJ and the eastward movement of the jet core and jet exit in the Pacific. With the movement of the STJ exit, the wave train tends to develop over the eastern region. The opposite is the case during La Niña when the westward shift of the jet exit favors the development of the wave train in the western region. Our findings expand the current understanding regarding ENSO teleconnection.

KEYWORDS: Rossby waves; Southern Hemisphere; Kinetic energy; Atmosphere-ocean interaction; ENSO; Asymmetry

1. Introduction

El Niño–Southern Oscillation (ENSO) is the dominant interannual air–sea coupling mode in the tropical Pacific. Its climatic impacts are not limited to the tropical Pacific, but also reach other tropical and extratropical regions, thereby impacting global climate variability (Hoerling et al. 1997; Trenberth et al. 1998; Gong et al. 2015; Tao et al. 2015; Xie et al. 2016; Jiang et al. 2017; Hu et al. 2017; Gong et al. 2018; Tao et al. 2018; Liu et al. 2019; Cai et al. 2019). ENSO modulates the extratropical climate through both zonally symmetric and asymmetric pathways. During El Niño years, the equatorial central-eastern Pacific warms, and the angular momentum delivered from the equator to the subtropics increases. Correspondingly, the Hadley cell (HC) strengthens and contracts with the equatorward shift and intensification of the subtropical jet stream (STJ; Rind et al. 2001; Robinson 2002; Lu et al. 2008). The opposite is the case with La Niña. Apart from the direct thermal response, ENSO also has an effect on the propagation and intensity of transient eddies, which induce poleward energy transport in the midlatitudes, leading to a zonally symmetric response as well (Seager et al. 2003; Lau et al. 2005). Many previous works have connected ENSO to the southern annular mode via the above mechanism (Seager et al. 2003; L'Heureux and Thompson 2006; Fogt et al. 2011).

Moreover, ENSO is capable of regulating the extratropical climate by zonally asymmetric stationary waves (Trenberth et al. 1998; Held et al. 2002; Liu and Alexander 2007). Anomalous tropical sea surface temperatures (SSTs) excite stationary Rossby wave trains that extend to extratropical regions (Held and Kang 1987). In the Northern Hemisphere, ENSO excites the Pacific–North America (PNA) teleconnection pattern, which manifests as a wave train structure from the tropical Pacific to North America, modulates the intensity of the Aleutian low and the high pressure center in western Canada, and favors extreme weather events over the southern United States (Hoerling et al. 1997). Likewise, an ENSO-related Pacific–South America (PSA) wave train is observed in the Southern Hemisphere (Karoly 1989; Mo and Higgins 1998; Mo and Paegle 2001). Previous studies have presented two PSA patterns in quadrature as being part of a propagating wave that can be excited by anomalous tropical convection (Mo and Higgins 1998; Mo and Paegle 2001).

The first PSA pattern is obtained from the second empirical orthogonal function mode of sea level pressure (SLP) or 500-hPa geopotential height in the Southern Hemisphere (Mo and Higgins 1998; Mo and Paegle 2001) and has a close relationship with ENSO (e.g., Schneider et al. 2012). The PSA wave train features three alternating anomalous pressure centers in the extratropics, extending from New Zealand to South America. The circulation anomalies of the wave train further

Corresponding author: Gang Huang, hg@mail.iap.ac.cn

DOI: 10.1175/JCLI-D-21-0285.1

influence the Amundsen Sea low, leading to a dipole pattern of surface air temperature anomalies over the Antarctic Peninsula and West Antarctica (Yuan and Martinson 2000; Yuan 2004; Ding et al. 2011; Li et al. 2014; Li et al. 2015; Wang et al. 2020). Previous studies have shown that the wave train is highly seasonally dependent, being more pronounced and intense in austral spring and winter than in summer (Jin and Kirtman 2009; Schneider et al. 2012; Ding et al. 2012; Yiu and Maycock 2019). According to Jin and Kirtman (2009), the PSA wave train's seasonal variation is primarily due to seasonal variation in the STJ, which favors the formation of the Rossby wave source.

However, the spatial pattern of the PSA wave train excited by ENSO seems to be nonstationary. Fogt and Bromwich (2006) indicated that the PSA mode moved eastward by 20° longitude in the 1990s owing to the eastward shift of the tropical convective position. In addition, Wilson et al. (2014, 2016) and Ciasto et al. (2015) found that the different types of ENSO can contribute to the wave shift. Specifically, Rossby waves excited by central Pacific (CP)-type El Niño shift westward owing to the westward movement of the tropical diabatic heating.

In this paper, the zonal asymmetry of the PSA wave train's response to different ENSO phases and the underlying mechanisms involved are further studied. The asymmetry has been noted by a few previous studies (e.g., Hitchman and Rogal 2010) but has not been systematically investigated using multiple sets of reanalysis and model data. The tropical heating regions are primarily regarded in previous studies as an important factor contributing to the asymmetry (Hoerling et al. 1997; Mo et al. 1998; Fogt and Bromwich 2006; Ciasto et al. 2015). However, it remains unclear if other pathways would lead to the zonal movement of the wave trains.

Simmons et al. (1983) demonstrated that the STJ plays an important role in the development of the disturbance in the subtropics via barotropic energy conversion. Subsequently, a number of studies have further reported that the STJ exit region might anchor the location of the tropical heating–excited wave train (e.g., Ting and Yu 1998). In this paper, we investigate whether the asymmetry of the ENSO teleconnection is related to the STJ, and how the STJ leads to the asymmetry from the perspective of energy conversion (Simmons et al. 1983; Kosaka and Nakamura 2006; Hu et al. 2019). As the present study mainly focuses on how the STJ modulates the wave train, the austral winter season—when the STJ is strongest and closest to the equator—is chosen. Similar results are also identified in austral spring (figures not shown).

The rest of the paper is organized as follows. Section 2 introduces the data and models. Section 3 presents the observed asymmetric ENSO-excited teleconnection waves, as well as those simulated by atmospheric general circulation model (AGCM) experiments. The mechanism that leads to the asymmetry is presented in section 4. Section 5 provides a summary of our key findings.

2. Data and models

In this study, the monthly mean geopotential height data are from the NCEP–DOE AMIP-II reanalysis (NCEP-2; resolution: 2.5° × 2.5°; Kanamitsu et al. 2002) and ECMWF interim reanalysis (ERA-Interim; resolution: ~0.7° × 0.7°; Berrisford et al. 2011) from 1979 to 2015, and the ECMWF's first atmospheric reanalysis of the twentieth century (ERA-20C; Poli et al. 2016) from 1920 to 2010. The global gridded monthly SST datasets from the Hadley Centre Sea Ice and Sea Surface Temperature (HadISST) dataset for the period 1920–2015 (Rayner et al. 2003) are also utilized. As we mainly focus on the impact of ENSO on the PSA wave train in austral winter, ENSO is measured by the June–August (JJA) mean Niño-3.4 (5°S–5°N, 170°–120°W) SST index. For the reanalysis datasets in the contemporary era (1979 to date), ENSO events are identified following the criteria used by NCEP's Climate Prediction Center. For ERA-20C (1920–2010), an El Niño event is defined as when the Niño-3.4 index is greater than one standard deviation of the SST anomalies, and a La Niña event as when the index is less than one standard deviation. Composite analysis and Pearson correlation coefficients are used in the study, and the statistical significance is evaluated by the two-tailed Student's t test and bootstrap testing with 1000 resamplings.

The Max Planck Institute for Meteorology AGCM (ECHAM5.3.2) is employed in this study, with triangular truncation at zonal wavenumber 63 (T63; equivalent to a horizontal resolution of 1.9°) and 31 vertical levels. ECHAM5.3.2 has been proven to perform well in the simulation of ENSO-related climate anomalies (e.g., Liu et al. 2018, 2019). A detailed description of the model can be found in Roeckner et al. (2003).

The linear baroclinic model (LBM) used in this study is based upon primitive equations linearized over a given basic state. A dry version of the LBM with a horizontal resolution of T42 and 20 sigma levels and schemes for horizontal and vertical diffusion, Rayleigh friction, and Newtonian damping is utilized. More details of the model are presented in Watanabe and Kimoto (2000). To yield a stable atmospheric response to the heating source, the model is integrated for 50 days, and averages from 20 to 50 days are adopted for investigation.

3. Asymmetric responses of El Niño and La Niña

a. Reanalysis

Figure 1a shows the composite JJA 200-hPa geopotential height anomalies during El Niño years (1982, 1987, 1991, 1997, 2002, 2004, 2009, and 2015). A Rossby wave train–like pattern can be observed over the southern Pacific. The wave train propagates southward to the subtropics and then southeastward to the Antarctic Peninsula. The structure and pathway are in good agreement with the PSA teleconnection pattern proposed in many previous studies (Karoly 1989; Mo and Higgins 1998; Mo and Paegle 2001). Similar to El Niño, the atmospheric response in La Niña years (1985, 1988, 1998, 1999, 2000, 2007, 2010, and 2011) presents a PSA-like wave but for an almost opposite phase (Fig. 1b). However, the location of geopotential height anomalies around the Amundsen Sea and downstream regions are not symmetrical between El Niño and La Niña years. The anomalous center during El Niño is situated far to the east relative to La Niña (Figs. 1a,b). Similar asymmetric features are captured by using ERA-Interim and ERA5 data (figures not shown), albeit with some discrepancies in the intensity of the

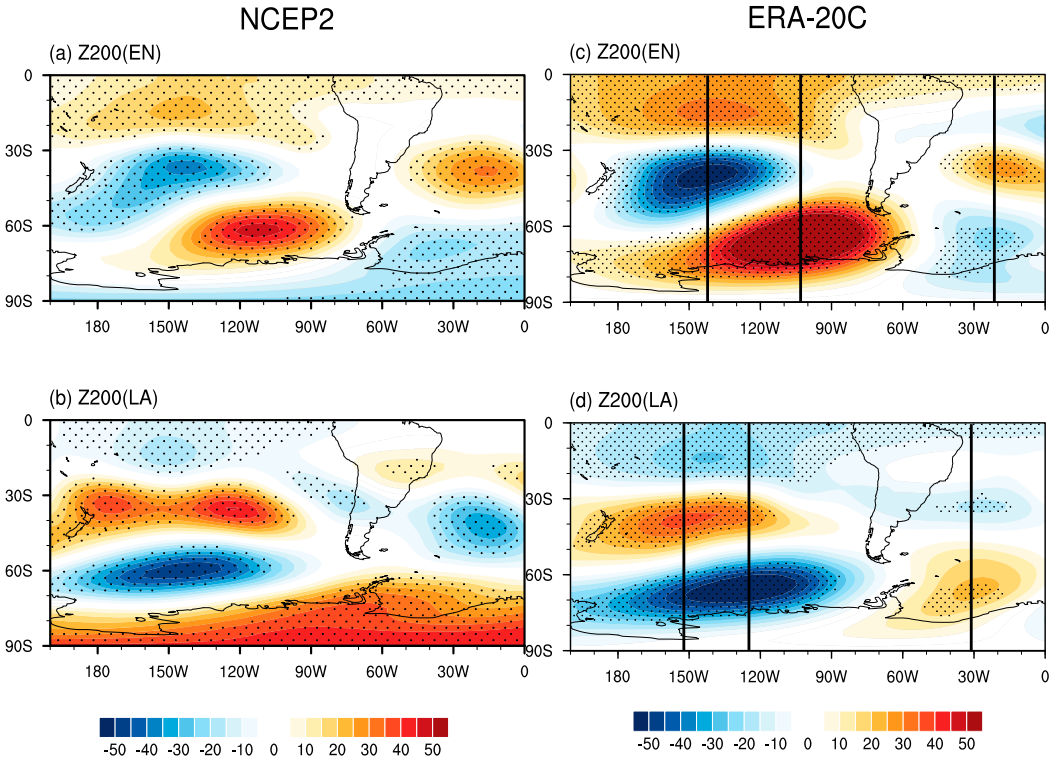

FIG. 1. Composites of the JJA-mean 200-hPa geopotential height (colors; unit: m) during (a),(c) El Niño and (b),(d) La Niña years, showing results for (left) NCEP-2 and (right) ERA-20C. The dots show where the composites are significantly different from the climatology at the $p < 0.01$ confidence level based on a bootstrap test. The vertical lines indicate the longitudes of the anomalous centers in the mid- and high latitudes in the Pacific and South Atlantic.

geopotential height anomalies between ERA-Interim and NCEP-2. When further analyzing the ERA-20C data from 1920 to 2010, more robust zonal-movement features can be identified (Figs. 1c,d). The difference between the two composites is statistically significant ($p < 0.01$) as tested by the bootstrap method, suggesting the asymmetry is robust. Moreover, with the long-term dataset, we find the shift of the wave train is not limited to the high latitudes but emerges from the subtropics.

The asymmetric responses of the PSA pattern in turn cause asymmetric climate patterns in Antarctica. Figure 2 shows the composite SAT anomaly for both positive and negative phases based on ERA-20C. During El Niño years, a dipole in SAT anomalies exists between West Antarctica and the Antarctic Peninsula. Anomalous southerly winds advect cold air that cools the peninsula, and anomalous northerly winds advect warm air that warms West Antarctica. In contrast, during La Niña, the Antarctic Peninsula experiences only a minor temperature change. The difference is mainly attributable to the westward shift of the anomalous center in the Amundsen Sea during La Niña years.

b. AGCM solution

Utilizing ECHAM5.3.2, five sets of experiments with different boundary conditions are designed to investigate the asymmetric nature. The control run (CTL) is forced by the fixed climatological boundary conditions, including the climatological monthly SST and sea ice from 1980 to 2005. The other four experiments are the El Niño composite SST experiment (EN_composite), La Niña composite SST experiment (LA_composite), El Niño idealized SST experiment (EN_id), and La Niña idealized SST experiment (LA_id). The EN_composite experiment is forced by the SSTs that add monthly composite SST anomalies (Fig. 3a) for the selected El Niño years to the climatological SST for every calendar month. The same is the case for the LA_composite experiment, except for being forced by La Niña composite SST (Fig. 3b). EN_id and LA_id experiments are forced by positive and negative idealized symmetric SST anomalies (Fig. 4) following Trascasa-Castro et al. (2019), which are imposed as follows:

$$\Delta T(\lambda,\varphi) = \begin{cases} \alpha \arctan\left(\dfrac{\lambda - 180^\circ}{6}\right)\exp\left[-0.03(\varphi^2)\right], & \text{if } 180^\circ \le \lambda \le 285^\circ \text{ and } -10^\circ \le \varphi \le 10^\circ \\ 0, & \text{otherwise} \end{cases}. \quad (1)$$

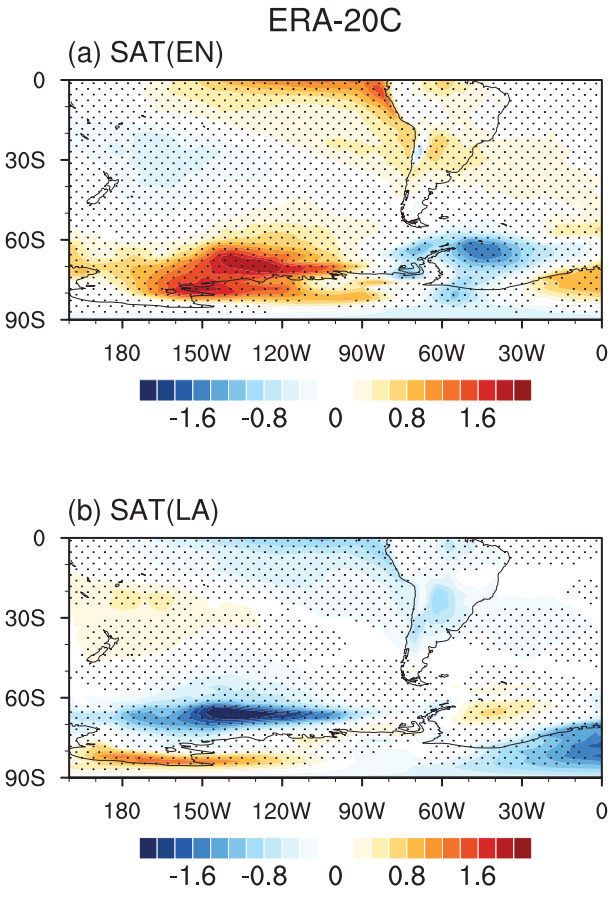

FIG. 2. Composites of JJA-mean SAT anomalies (colors; unit: °C) during (a) El Niño and (b) La Niña years in ERA-20C.

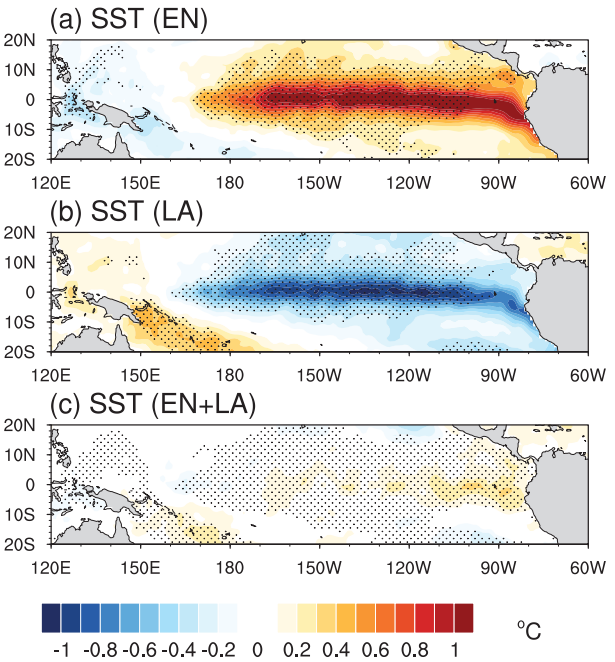

FIG. 3. Composite JJA SST (HadISST) anomalies during (a) El Niño (1982, 1987, 1991, 1997, 2002, 2004, 2009, 2015) and (b) La Niña (1985, 1988, 1998, 1999, 2000, 2007, 2010, 2011) years. (c) Sum of the composite SST anomalies between El Niño and La Niña events. The dots in (a) and (b) show where the SST is significantly different from the climatology at the 5% confidence level, while the dots in (c) show where the SST composites are significantly different between El Niño and La Niña events at the 5% confidence level as tested by the bootstrap method.

The constant α in Eq. (1) is a scaling factor that controls the intensity of the SST anomalies. In the EN_id run, α is set to 1.15, yielding an El Niño–like pattern with the Niño-3.4 index equaling 1.5 K. In the LA_id run, meanwhile, the La Niña–like pattern with the Niño-3.4 index equaling −1.5 K is generated by setting α to −1.15. Although the SSTs are imposed with an idealized function, they have a high degree of similarity to the observed ENSO SST (Trascasa-Castro et al. 2019; Yiu and Maycock 2019). Each experiment is integrated for 21 years, with the final 20 years utilized for analysis. Thus, each simulation is equivalent to a 20-member ensemble run.

Figures 5a and 5b show the 200-hPa geopotential height anomalies of EN_composite minus CTL and LA_composite minus CTL, respectively. In response to El Niño SST anomalies, there is a positive Gill pattern in the tropical Pacific and an arch-like wave train from the central Pacific to the Antarctic Peninsula and to the South Atlantic. The 200-hPa circulation pattern in response to La Niña SST anomalies also features an arch-like wave train from the central Pacific to the South Atlantic, but shifts westward relative to the pattern excited by El Niño. The result suggests that the AGCM can capture the asymmetric response of the PSA pattern to El Niño and La Niña SST anomalies. Nevertheless, the composite SST anomalies vary in both distribution and intensity (Fig. 3c); the intensity of El Niño events is 0.1–0.4 K larger over the eastern Pacific relative to La Niña, leading to difficulties in attribution. Several studies have shown that the different types

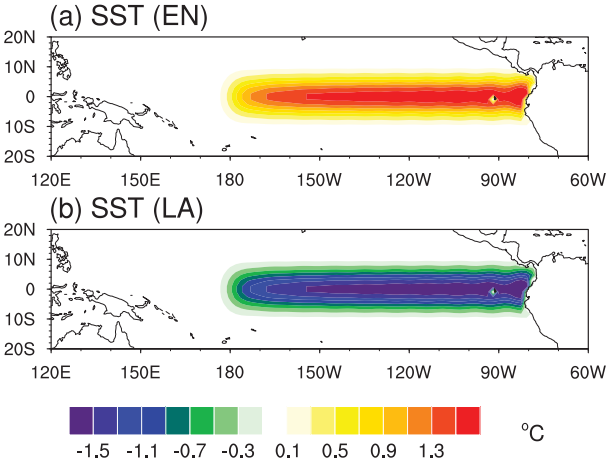

FIG. 4. The imposed (a) 1.5-K El Niño and (b) −1.5-K La Niña perturbations in the EN_id and LA_id experiments, respectively.

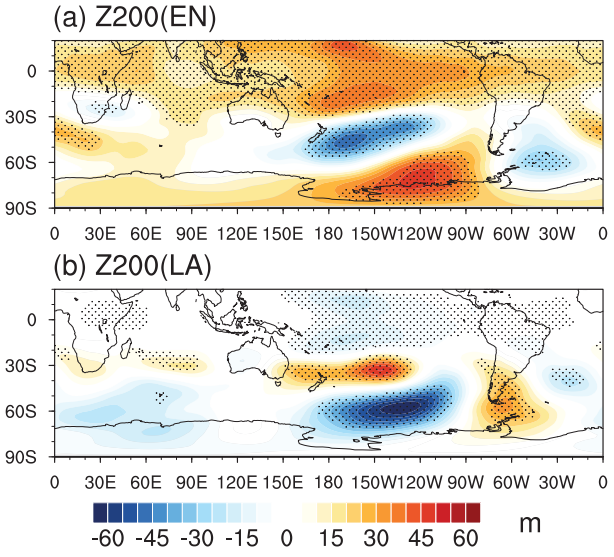

FIG. 5. JJA-mean 200-hPa geopotential height anomalies (unit: m) in the (a) EN_composite and (b) LA_composite experiments forced with composite SSTAs. The dots show where the atmospheric anomalies are significantly different from CTL at the $p < 0.05$ confidence level according to the Student's t test.

of ENSO spatial pattern (e.g., CP and eastern Pacific El Niño) and intensity (e.g., moderate and extreme El Niño) result in vastly different atmospheric responses (e.g., Ciasto et al. 2015; Johnson and Kosaka 2016). Thus, we use EN_id and LA_id experiments to determine whether the asymmetry results solely from the phase change of the SST anomalies.

Figure 6 presents the 200-hPa geopotential height and SLP anomalies for EN_id run minus CTL run and LA_id run minus CTL run. Similar to the reanalysis data, the experiments identify baroclinic Gill-like patterns in the tropics and barotropic PSA-like teleconnections over the extratropics (Fig. 6). The similarity between the simulated and observed wave trains indicates that the ECHAM5.3.2 experiments imposed by idealized SSTs are applicable to study the observed atmospheric responses to ENSO in the Southern Hemisphere.

Furthermore, the model results reproduce the asymmetric atmospheric responses to El Niño and La Niña. In the EN_id experiment, the subtropical Pacific geopotential height anomaly extends more to the east relative to the LA_id run (Figs. 6a,b). In the downstream region, the anomaly distributed over the Amundsen Sea extends to the western flank of the Antarctic Peninsula, which is far to the east compared with that in the LA_id run (Figs. 6c,d). The eastward movement of the atmospheric responses in the Amundsen Sea and Atlantic sector in the EN_id run is consistent with that in the reanalysis (Fig. 1). Note that the shift is not limited to local areas at high latitudes as it is in NCEP-2 with limited samples (Fig. 1), but instead originates from the subtropics in the model results, which is in agreement with the long-term reanalysis (ERA-20C). The differences between the composites are statistically significant ($p < 0.05$) over anomalous centers as determined by the Student's t test. The above model experiment results confirm the asymmetric responses of the PSA wave train to El Niño and La Niña.

4. Mechanisms of asymmetry

a. Asymmetric response of the STJ to El Niño and La Niña

Previous works have demonstrated the critical role of the STJ in the growth of Rossby waves excited by ENSO (Simmons et al. 1983; Jin and Kirtman 2009; Ji et al. 2016; Yiu and Maycock 2019). Figures 7a and 7b present the zonal-mean zonal wind anomalies during El Niño and La Niña years in the NCEP-2 data. The responses of the zonal-mean zonal winds to ENSO bear close resemblance to previous studies

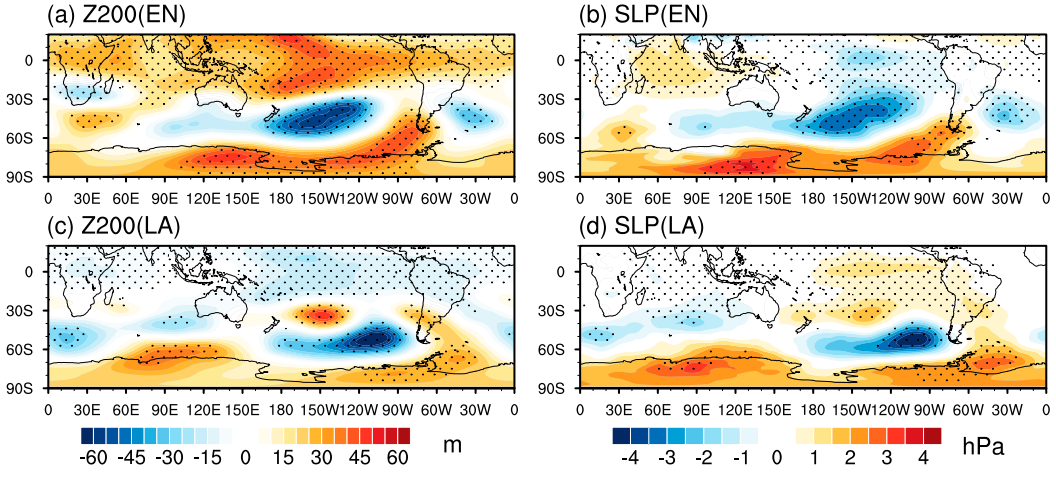

FIG. 6. JJA-mean 200-hPa geopotential height anomalies (unit: m) in (a) EN_id and (c) LA_id experiments, and the SLP anomalies (unit: hPa) in (b) EN_id and (d) LA_id ECHAM5.3.2 simulations. The dots show where the atmospheric anomalies are significantly different from CTL at the $p < 0.05$ confidence level according to the Student's t test.

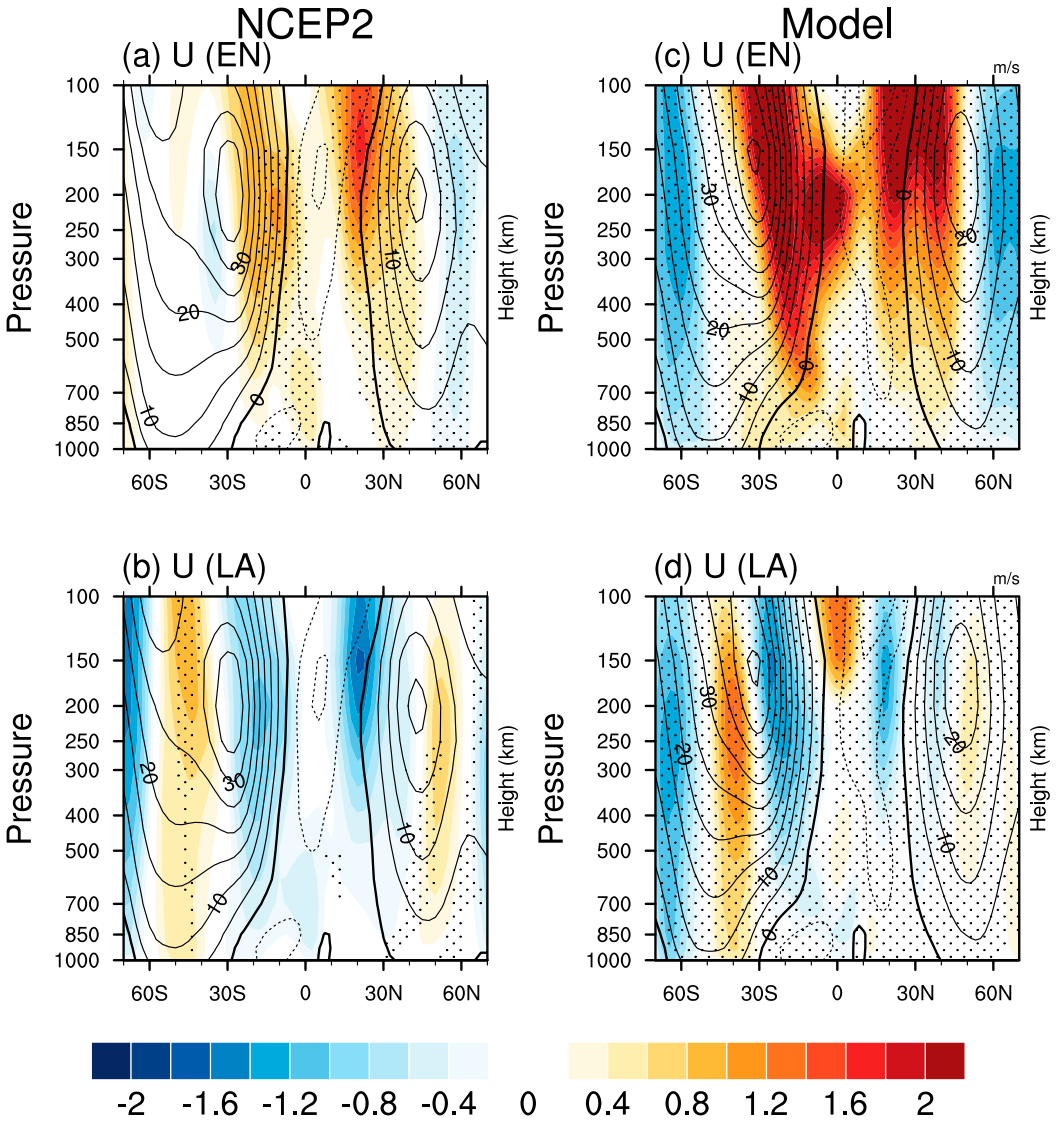

FIG. 7. JJA-mean 200-hPa zonal-mean zonal wind anomalies (colors; unit: m s^{-1}) in (a),(c) El Niño and (b),(d) La Niña (contour lines show the climatology) based on (a),(b) NCEP-2 and (c),(d) EN_id and LA_id simulations. The dots show where anomalies are significantly different from the climatology at the $p < 0.05$ confidence level according to the Student's t test.

(Lu et al. 2008; Robinson 2002). During El Niño years, the upper-level zonal winds intensify near the equatorial flank of the STJ, leading to a strengthening and equatorial movement of the jet, whereas in La Niña years the jet is weakened and shifts poleward owing to the weakening of the zonal wind near the equatorial flank of the STJ. The right-hand panels in Fig. 7 show the zonal-mean zonal wind anomalies in EN_id and LA_id experiments. The results are highly similar to those based on NCEP-2, showing a strengthening and equatorial shift of the STJ in the EN_id run and a weakening and poleward shift in the LA_id run. Note that the simulated wind anomalies in the model are stronger than those seen in the reanalyses. The difference mainly comes from the varying intensity of the composite observed SST and the idealized SST imposed in the model. The latter is about 0.5 K larger than the former.

The responses of the zonal-mean zonal winds coincide with the variations of the HC. Figure 8a displays the differences in the zonal-mean mass streamfunction between El Niño and La Niña during JJA in NCEP-2. The climatological HC is seen in the winter hemisphere, accompanied by the anomalous upward branch at 10°N and downward branch at 30°S. In El Niño, the HC is enhanced and contracted owing to the anomalous positive convective heating in the tropics, and is weakened and expanded because of the negative convective heating during La Niña, which is in agreement with previous studies (e.g., Lu et al. 2008; Rind et al. 2001). The model experiments successfully capture the characteristics of the HC's response to El Niño and La Niña (Fig. 8b). The enhanced HC coincides well with the strengthening of the STJ in Fig. 7, whereas the weakened HC coincides with the weakened STJ, indicating enormous differences in the

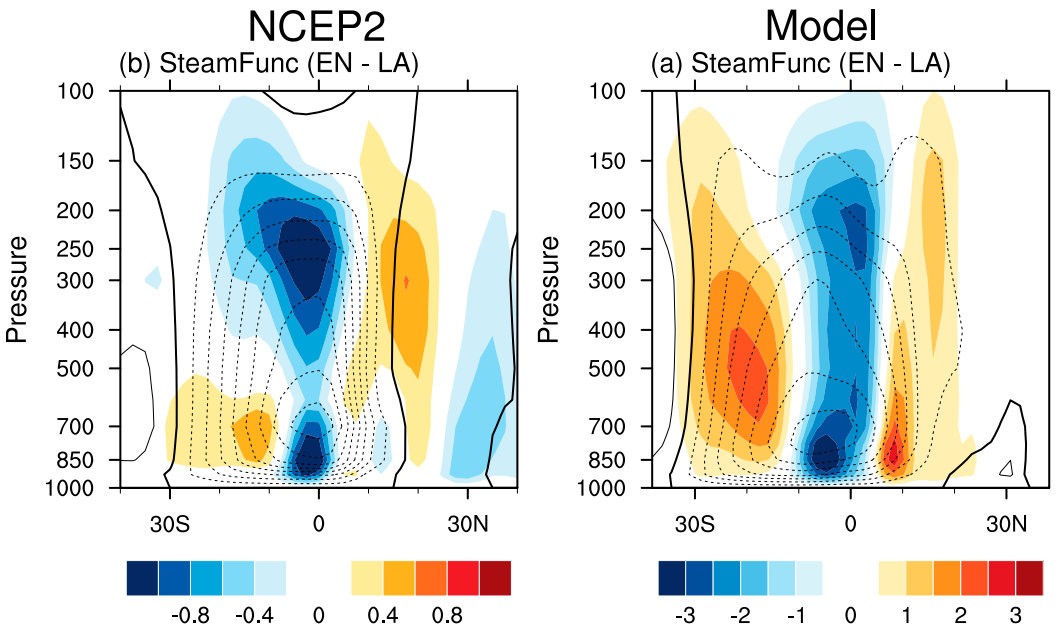

FIG. 8. Differences in JJA zonal-mean mass streamfunction (colors; unit: 10^{10} kg s^{-1}) between El Niño and La Niña in (a) NCEP-2 and (b) ECHAM5.3.2 simulations forced by idealized SST. The contour lines show the climatology.

structure of large-scale atmospheric circulation during El Niño and La Niña.

The spatial distribution of the 200-hPa zonal winds for EN_id and LA_id experiments is shown in Fig. 9, and the composite maps of zonal winds in NCEP-2 (figures not shown) are similar to the model simulations. For the EN_id experiment, the STJ in the Pacific is intensified, with the strongest zonal winds ($u > 50$ m s^{-1}) extending eastward to near 150°W. For the LA_id run, the STJ weakens and the jet core shifts 30° longitude to the west relative to the EN_id run. The change in the STJ during El Niño and

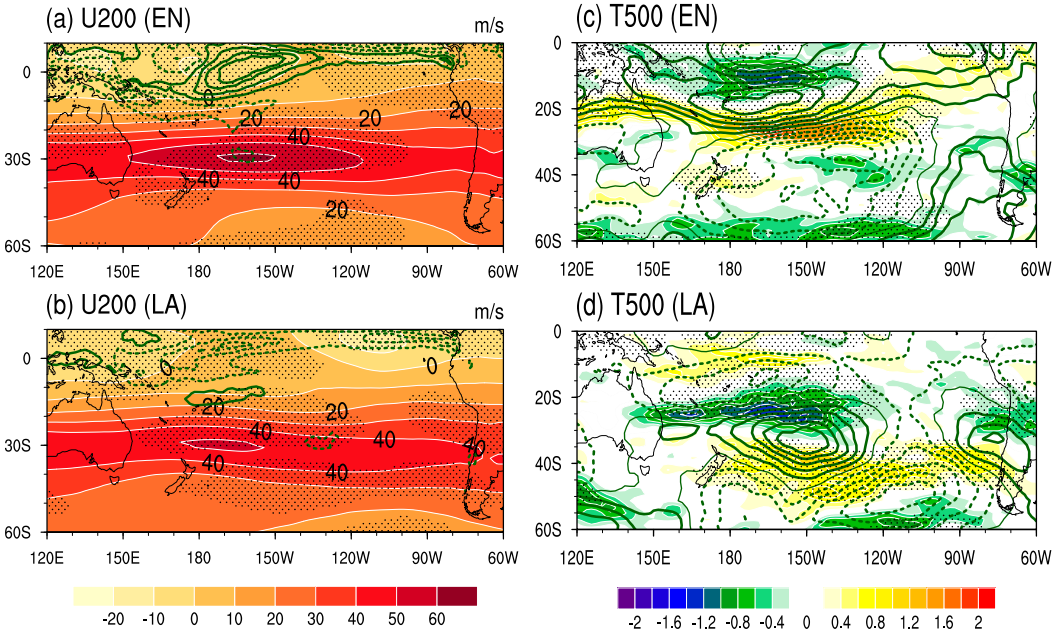

FIG. 9. JJA-mean 200-hPa zonal winds (colors; unit: m s^{-1}) and precipitation (contours; unit: mm day^{-1}) in (a) EN_id and (b) LA_id runs in ECHAM5.3.2, and JJA-mean 500-hPa temperature anomalies (contours) and meridional temperature gradient (colors; unit: °C) in (c) EN_id and (d) LA_id runs. The dots show where atmospheric anomalies are significantly different from CTL at the $p < 0.05$ confidence level according to the Student's t test.

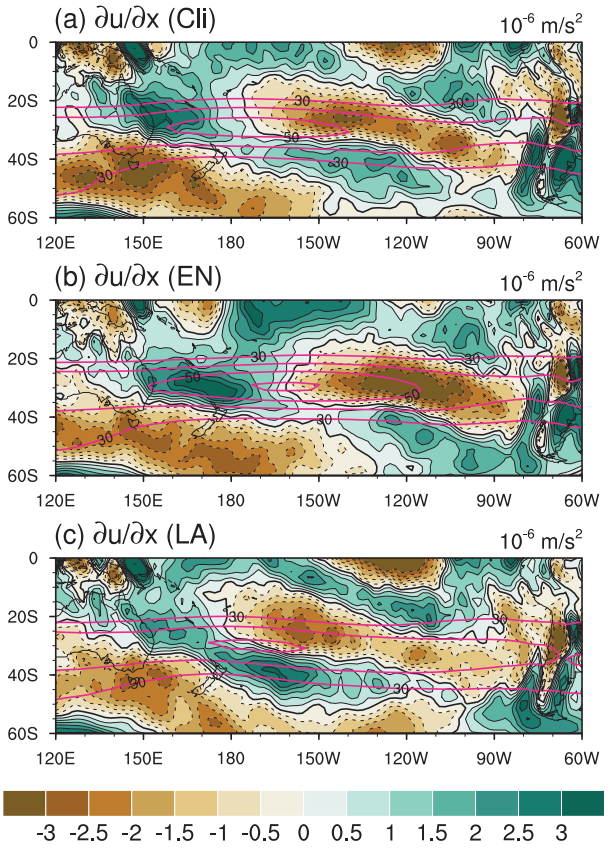

FIG. 10. JJA-mean $\partial U/\partial x$ of (a) CTL, (b) EN_id and (c) LA_id experiments in ECHAMN5.3.2 at 200 hPa. Solid lines present the 200-hPa zonal winds.

La Niña is consistent with the HC (Fig. 8) and the zonal-mean zonal winds (Fig. 7). The responses of the Pacific STJ core to ENSO are consistent with many previous studies in the Northern Hemisphere (Yang and Webster 1990; Hoerling et al. 1997; Mo et al. 1998).

As reported by Yang and Webster (1990) and Rind et al. (2001), the change in the STJ is largely controlled by the convective precipitation anomalies and meridional temperature gradient in the tropics (Fig. 9). Specifically, the precipitation anomalies during El Niño induce positive anomalous diabatic heating in the central and eastern Pacific, increasing the meridional temperature gradient in the central subtropical Pacific, which results in positive zonal winds in this region; During La Niña, the negative diabatic heating induces a decrease in the meridional temperature gradient, and the zonal winds in the central subtropical Pacific simultaneously decrease. With the shift of the strongest zonal winds, the Pacific jet exit region where the zonal winds are confluent accordingly moves in the zonal direction (Fig. 10).

b. *Effect of the asymmetric STJ on the movement of the PSA teleconnection pattern*

The asymmetry of the PSA teleconnection pattern is accompanied by the movement of the STJ core and jet exit region (Figs. 9a,b), suggesting a potential relationship between the STJ and PSA pattern. Simmons et al. (1983) pioneered the idea that barotropic energy conversion between the basic mean flow and perturbations in the Pacific STJ exit region plays an important role in the formation of the PNA pattern. The present study investigates the contributions of the STJ to the asymmetric response of the PSA to El Niño and La Niña from a barotropic energy conversion perspective.

As explained in Kosaka and Nakamura (2006), the barotropic growth of the local kinetic energy (KE) associated with perturbations from the basic state can be given by

$$\frac{\partial \mathrm{KEH}}{\partial t} \approx \underbrace{\frac{(v'^2 - u'^2)}{2}\left(\frac{\partial u_b}{\partial x} - \frac{\partial v_b}{\partial y}\right)}_{\mathrm{CK}_x} - \underbrace{u'v'\left(\frac{\partial u_b}{\partial y} + \frac{\partial v_b}{\partial x}\right)}_{\mathrm{CK}_y}, \qquad (2)$$

where KEH is horizontal perturbed kinetic energy, and CK is the conversion of local kinetic energy from the basic state to

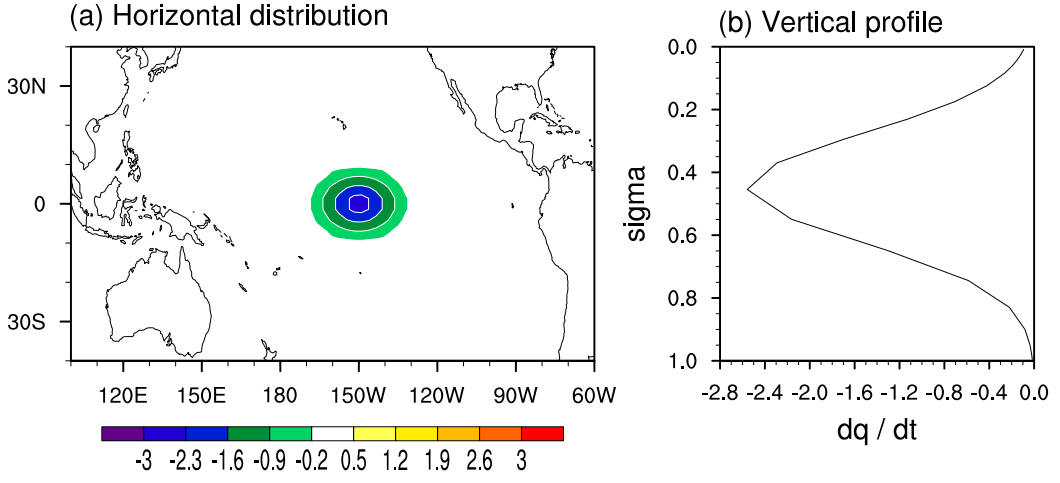

FIG. 11. (a) Horizontal distribution and (b) vertical profile of imposed atmospheric diabatic heating (K day^{-1}) in the central Pacific in the two LBM experiments.

perturbations, u' and v' represent the anomalous zonal and meridional winds, respectively, and u_b and v_b denote the climatological winds. As discussed in Simmons et al. (1983), CK can be represented with good accuracy as $CK = \mathbf{E} \cdot \nabla_H \bar{u}$, where $\mathbf{E} = (v'^2 - u'^2, -u'v')$ is the extended Eliassen–Palm (EP) vector (Hoskins et al. 1983).

Based on Eq. (2), the dominant processes by which the growing disturbances extract KE from the basic state (CK) can be described by two conversion terms: CK_x and CK_y. In the jet exit, where the zonal wind diverges into a broad region, $\partial u_b/\partial x$ is strongly negative. Thus, zonally elongated circulation anomalies ($u'^2 > v'^2$) can readily extract positive CK_x in the STJ exit region according to Eq. (2). Similarly, northeast–southwest-tilted circulation anomalies are conducive to the extraction of positive CK_y in the northern vicinity of the STJ where $\partial u_b/\partial y$ is strongly negative. Hence, the conversion of KE depends on both the distribution of the mean circulation and the morphology of the disturbance. As the upstream disturbance is mostly zonally elongated, CK_x is more important than CK_y, which has also been confirmed by previous studies for the Northern Hemisphere (e.g., Kim et al. 2020).

Figure 10 presents the horizontal distribution of $\partial U/\partial x$ and zonal winds at 200 hPa. In Fig. 10a, the minimum of $\partial U/\partial x$ in the subtropics is distributed between 150° and 110°W in the climatological STJ exit region. As the STJ moves eastward, the region with the minimum value of $\partial U/\partial x$ in which anomalies could develop most efficiently shifts eastward, indicating that the disturbance is more prone to growing over the southeastern Pacific in the EN_id run (Fig. 10b). The movements of the STJ and PSA are coupled with each other in the EN_id run, whereas for the LA_id run the region with the minimum value of $\partial U/\partial x$ moves westward, matching the westward shift of the perturbation in Fig. 6b. Similar results are obtained based on NCEP-2 data (figures not shown).

Note that the locations of both the STJ exit and the anomalous tropical precipitation vary between the observations and ECHAM5.3.2 simulations. It is difficult to identify which factor contributes to the movement of the wave train. We can easily change the background state of the LBM model, which is linearized over a fixed basic state, in order to study the causal mechanism by which varying STJ contributes to different atmospheric responses forced by the same heating source. As the basic mean state is kept constant, we can examine the role of the barotropic energy conversion in the STJ exit in the development of the disturbance over the Southern Hemisphere in JJA.

Two LBM experiments are set up to examine whether the position of the STJ exit affects the movement of the disturbance. The settings of the two experiments are identical except for the basic mean circulation. The observed JJA climatology is used for the mean circulation in the first experiment (EXP1). In the second experiment (EXP2), the climatological basic flow is shifted 20° to the west, similar to the westward shift of the Pacific STJ in La Niña years. The prescribed heating source has a cosine elliptical pattern, with a peak of -3 K day^{-1} at the 0.45 sigma level, mimicking the effect of the anomalous negative heating during La Niña summers. The horizontal distribution and the vertical profile of the heating source are presented in Fig. 11. Other heating sources with different intensities and locations (e.g., centered on 170°W) are also tested, and similar results are obtained (figures not shown).

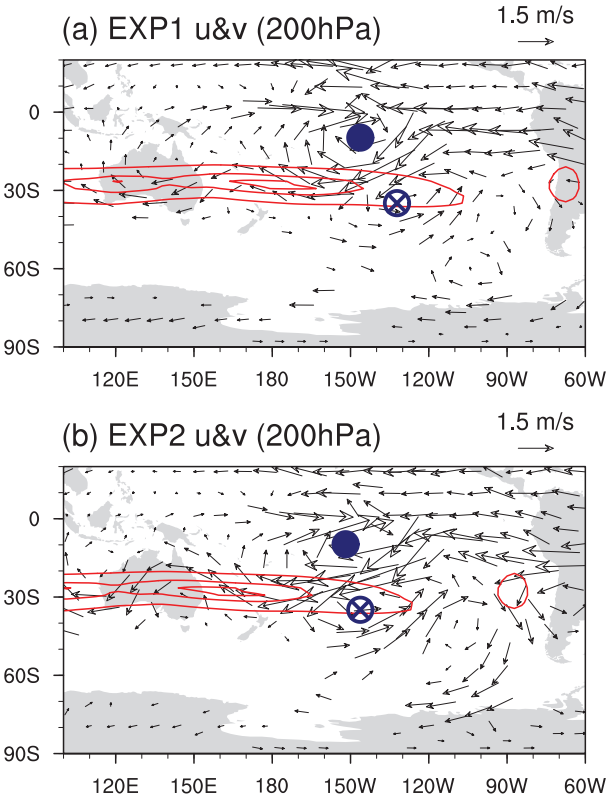

FIG. 12. The 200-hPa wind (vectors; unit: m s^{-1}) responses and the climatological zonal winds (contours; unit: m s^{-1}) in LBM experiments with (a) the climatological basic flow and (b) the basic flow shifted 20° to the west. The solid circle represents the center of the 200-hPa tropical geopotential height response and the open circle represents the center of the downstream extratropical system. The areas with statistically significant ($p < 0.05$) differences in the wind responses according to the Student's t test are displayed.

Figure 12 describes the 200-hPa wind responses in the two experiments. The wind responses in both experiments feature a PSA-like wave train in the negative phase. An anticyclonic circulation is distributed in the tropics, followed by a wave train propagating southward from the subtropics, causing an anticyclonic anomaly in the vicinity of the Antarctic Peninsula. The result is similar to that in observations and the AGCM. Furthermore, we find that the disturbance in the subtropics moves westward as the STJ shifts 20° to the west (Fig. 12b). In EXP1, forced with the climatological mean circulation, the subtropical disturbance is located between 150° and 110°W, at the exit of the STJ, while in EXP2, in which the basic flow is shifted 20° to the west, the disturbance shifts westward to between 170° and 130°W.

To further investigate the relationship between the STJ and the disturbance, the CK is calculated. The CK and CK_x at

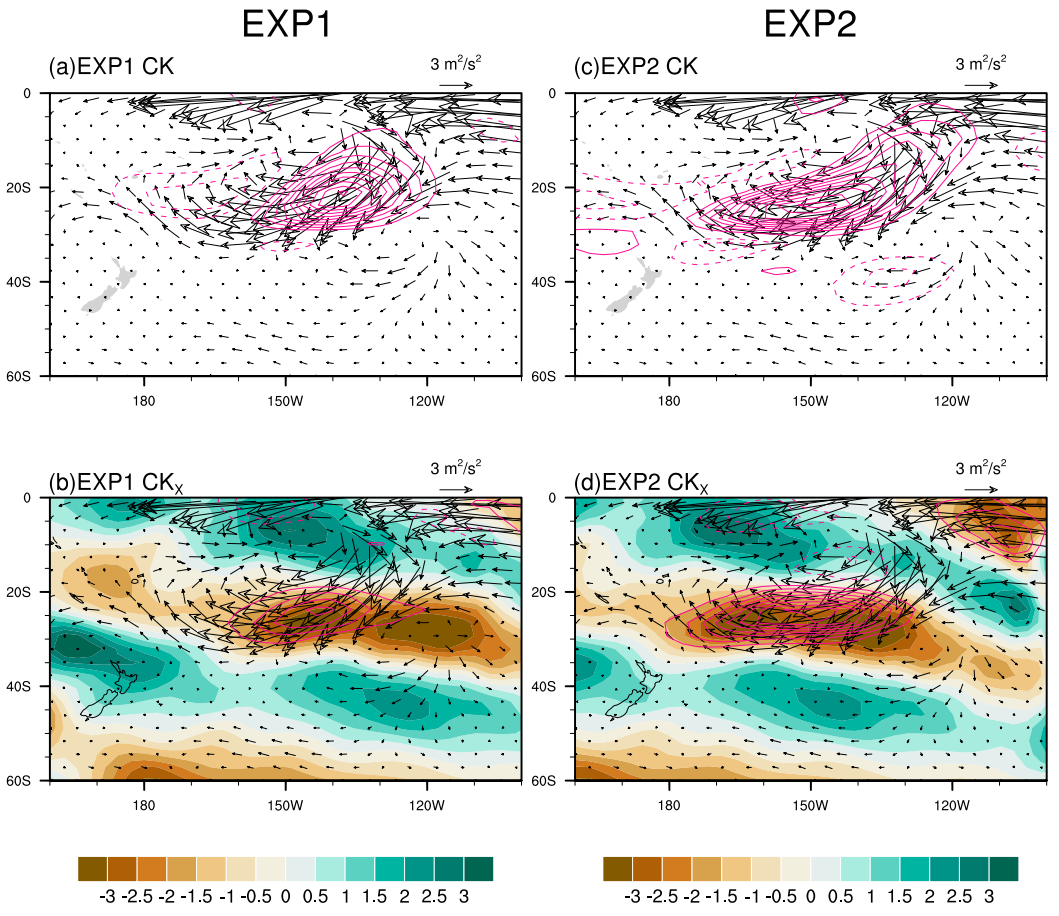

FIG. 13. (a),(c) Local barotropic energy conversion (contours; $\times 10^{-6}$ m^2 s^{-3}) at 200 hPa and (b),(d) CK$_x$ with contour intervals of 5 (-10, -5, 0, …), forced with (a),(b) the climatological basic flow and (c),(d) the basic flow shifted 20° to the west. The extended EP vector (arrows with scaling at the top of each panel) and $\partial\overline{u}/\partial x$ of the climatology [colors in (b) and (d)] are also presented.

200 hPa in the LBM experiments are presented in Fig. 13. CK is positive in the tropics and subtropics but weakly negative in the midlatitudes over the Pacific sector in EXP1 (Fig. 13a). Pronounced positive CK in the tropical Pacific results from the southwest–northeast-tilted anomalies ($u'v' > 0$) at the northern flank of the STJ $\left[(\partial\overline{u}/\partial y) < 0\right]$, which indicates that CK$_y$ is dominant in the tropics. The southwest–northeast-tilted anomalies ($u'v' > 0$) in the tropics are also manifested by **E** pointing to southern regions. The positive CK in the subtropics is primarily contributed by CK$_x$ in the exit region of the STJ (Fig. 13b). In this exit region $\left[(\partial\overline{u}/\partial x) < 0\right]$, where the minimum of $\partial\overline{u}/\partial x$ is distributed, the zonally elongated anomalies induce positive CK (**E** is pointing to the west). The consistency of the distribution of the strong positive CK$_x$ and the anomaly indicates that the positive barotropic energy conversion, especially CK$_x$, contributes to the development of the disturbance in the STJ exit region. The results are further confirmed in EXP2 in which the basic flow is shifted 20° to the west. In the tropics, the CK in EXP2 (Fig. 13c) is similar to that in EXP1, suggesting that CK$_y$ is largely unchanged, which corresponds to the consistent tropical responses in both experiments (Fig. 12). However, the CK$_x$ distributed in the subtropics is situated more to the west compared with that in EXP1, extending to the date line (Fig. 13d). The westward movement of CK$_x$ is consistent with the shift of the Pacific STJ and the related exit region $\left[(\partial\overline{u}/\partial x) < 0\right]$. As the STJ shifts westward, the disturbance is more likely to extract KE from the western region, leading to the westward movement of the atmospheric anomalies (Fig. 12b).

c. *Role of the asymmetric location of anomalous convective precipitation*

The above results demonstrate that the shift of the Pacific STJ exit region induces the movement of the tropical heating–excited wave trains. With many previous studies indicating that varying tropical heating locations play a significant role in the zonal shift of the ENSO teleconnection (e.g., Hoerling et al. 1997; Mo et al. 1998), one might ask which contributes more to the movement of the wave train—the heating source, or the STJ exit region? An additional LBM experiment is established to further investigate how heating sources with different locations impact the wave trains. The heating source imposed in

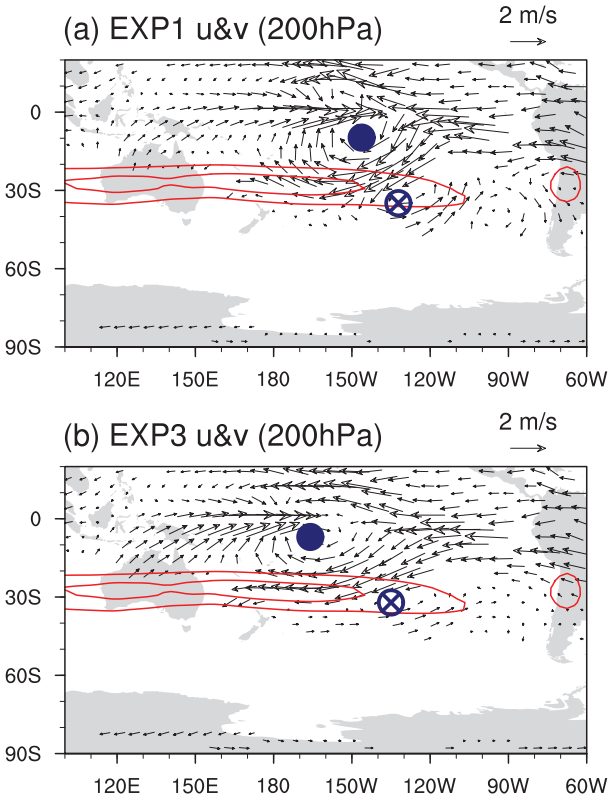

FIG. 14. The 200-hPa wind (vectors; unit m s^{-1}) responses and the climatological zonal winds (contours; unit: m s^{-1}) in (a) EXP1 and (b) EXP3. The solid circle represents the center of the 200-hPa tropical geopotential height response and the open circle represents the center of the downstream extratropical system. The areas with statistically significant ($p < 0.05$) differences in the wind responses according to the Student's t test are displayed.

this extra experiment (EXP3) moves 20° to the west, centered on 170°W, but shares the same mean circulation as EXP1. Figure 14 presents the atmospheric responses in EXP1 and EXP3. With the shift of the heating source, the tropical Gill pattern moves substantially to the west in EXP3 relative to EXP1. However, the position of the extratropical anomaly remains anchored in the STJ exit region, consistent with that in EXP1. Moreover, another experiment with the heating source centered at 160°W is performed for comparison. The longitudes of the geopotential height centers in the tropics and extratropics are displayed in Table 1. As the heating source gradually moves westward, the tropical response moves accordingly. However, the downstream center barely moves, and is still located at the exit of the STJ.

The results suggest the importance of the STJ exit region in anchoring the location of the wave trains. Note that the LBM is only a linear dry model without a moist process or nonlinear feedback, and thus the above results should be taken with caution. Actually, some differences are apparent in the extratropical anomalies. The extratropical anomaly in EXP3 is weaker than that in EXP1, indicating that different heating locations do affect the wave trains. More experiments with AGCMs and coupled general circulation models should be conducted to further investigate this issue.

TABLE 1. Longitudes of the minimum center of the tropical response and the maximum center of the extratropical response of 200-hPa geopotential height for three experiments. The location of the imposed heating source in the three experiments is 150°, 160°, and 170°W, respectively.

Atmospheric response	Heating at 150°W	Heating at 160°W	Heating at 170°W
Tropics (20°S–0°, 180°–120°W)	146°W	155°W	166°W
Extratropics (40°S–20°S, 150°–110°W)	132°W	132°W	135°W

5. Conclusions

This study investigates the asymmetry of ENSO-related waves in the Southern Hemisphere in JJA and further explores the mechanisms from an energy conversion perspective. First, we systematically reveal the asymmetric nature of the ENSO teleconnection in the Southern Hemisphere using reanalysis datasets and model simulations. Composite analysis of the JJA 200-hPa geopotential height anomalies in both NCEP-2 and ERA-20C shows that anomalies over the Amundsen Sea in El Niño and La Niña years are not symmetrical (Fig. 1). During La Niña years, the anomaly is situated more to the west relative to that in El Niño years. The asymmetry of the ENSO-excited Rossby wave trains is reproduced by ECHAM5.3.2 forced with both composite and idealized symmetric SSTs (Figs. 5 and 6), implying that the result is robust and mainly arises from different ENSO phases. The asymmetric responses of the PSA pattern in turn cause asymmetric SAT anomalies in Antarctica.

Second, in addition to the traditional view that the asymmetry is attributable to differences in the tropical convective position, we find that the STJ can affect the location of the ENSO-excited PSA wave train teleconnection via barotropic energy conversion. During El Niño years, anomalous convective precipitation induces positive diabatic heating in the central and eastern Pacific, increasing the meridional temperature gradient, which in turn leads to strengthening of the STJ and eastward movement of the jet core and exit region (Fig. 9). With the STJ exit and its associated confluent region shifted eastward, the wave train tends to develop over the eastern region. The opposite is the case during La Niña when a westward shift of the jet exit favors the development of the wave train in the western region.

The above mechanism is further verified by LBM experiments (Figs. 12 and 13). We find that at the exit of the STJ, the zonally elongated anomalies can readily extract KE from the basic flow and develop efficiently in both experiments. In EXP1 with climatological circulation, the subtropical disturbance is located between 150° and 110°W, at the exit of the STJ; in EXP2, in which the basic flow is shifted to the west by 20°, the disturbance is more likely to extract KE from the western region, leading to westward movement of the atmospheric anomalies.

Moreover, based on the LBM model, we find that the STJ plays a more important role than the tropical convective heating in the wave movement. Although this comparison should be viewed with caution because of the model's idealized configuration, it nonetheless adds a new dimension to our understanding of the observed movement of the wave train. More experiments with AGCMs and coupled general circulation models should be conducted to further investigate this issue in the future. As both tropical anomalous convective heating (e.g., Zhou et al. 2014) and the STJ (e.g., Lu et al. 2008) change under global warming, it would be interesting to examine how and why ENSO teleconnections might change in the future.

Acknowledgments. The authors thank the three anonymous reviewers for their constructive and detailed comments. This study was jointly supported by the National Natural Science Foundation of China (42141019, 41831175, 41775086, 41661144016, 41706026, 41506003, and 41731173), the National Key R&D Program of China (2018YFA0605904), the Strategic Priority Research Program of Chinese Academy of Sciences (XDA20060502), the Key Deployment Project of the Centre for Ocean MegaResearch of Science, Chinese Academy of Sciences (COMS2019Q03), and the Youth Innovation Promotion Association of the Chinese Academy of Sciences (2021072). The authors declare no competing interests.

Data availability statement. The data that support the findings of this study are openly available at https://psl.noaa.gov/data/gridded/data.ncep.reanalysis2.html (NCEP-2; Kanamitsu et al. 2002) and https://www.ecmwf.int/en/forecasts/datasets/reanalysis-datasets/era-20c (ERA-20; Poli et al. 2016).

REFERENCES

Berrisford, P., and Coauthors, 2011: The ERA-Interim archive, version 2.0. ERA Rep. Series 1, 23 pp., https://www.ecmwf.int/sites/default/files/elibrary/2011/8174-era-interim-archive-version-20.pd.

Cai, W., and Coauthors, 2019: Pantropical climate interactions. *Science*, **363**, eaav4236 https://doi.org/10.1126/science.aav4236.

Ciasto, L. M., G. R. Simpkins, and M. H. England, 2015: Teleconnections between tropical Pacific SST anomalies and extratropical Southern Hemisphere climate. *J. Climate*, **28**, 56–65, https://doi.org/10.1175/JCLI-D-14-00438.1.

Ding, Q., E. J. Steig, D. S. Battisti, and M. Küttel, 2011: Winter warming in West Antarctica caused by central tropical Pacific warming. *Nat. Geosci.*, **4**, 398–403, https://doi.org/10.1038/ngeo1129.

——, ——, ——, and J. M. Wallace, 2012: Influence of the tropics on the southern annular mode. *J. Climate*, **25**, 6330–6348, https://doi.org/10.1175/JCLI-D-11-00523.1.

Fogt, R. L., and D. H. Bromwich, 2006: Decadal variability of the ENSO teleconnection to the high-latitude South Pacific governed by coupling with the southern annular mode. *J. Climate*, **19**, 979–997, https://doi.org/10.1175/JCLI3671.1.

——, ——, and K. M. Hines, 2011: Understanding the SAM influence on the South Pacific ENSO teleconnection. *Climate Dyn.*, **36**, 1555–1576, https://doi.org/10.1007/s00382-010-0905-0.

Gong, H., L. Wang, W. Chen, D. Nath, G. Huang, and W. Tao, 2015: Diverse influences of ENSO on the East Asian–western Pacific winter climate tied to different ENSO properties in CMIP5 models. *J. Climate*, **28**, 2187–2202, https://doi.org/10.1175/JCLI-D-14-00405.1.

——, ——, ——, R. Wu, G. Huang, and D. Nath, 2018: Diversity of the Pacific-Japan pattern among CMIP5 models: Role of SST anomalies and atmospheric mean flow. *J. Climate*, **31**, 6857–6877, https://doi.org/10.1175/JCLI-D-17-0541.1.

Held, I. M., and I. S. Kang, 1987: Barotropic models of the extratropical response to El Niño. *J. Atmos. Sci.*, **44**, 3576–3586, https://doi.org/10.1175/1520-0469(1987)044<3576:BMOTER>2.0.CO;2.

——, M. F. Ting, and H. L. Wang, 2002: Northern winter stationary waves: Theory and modeling. *J. Climate*, **15**, 2125–2144, https://doi.org/10.1175/1520-0442(2002)015<2125:NWSWTA>2.0.CO;2.

Hitchman, M. H., and M. J. Rogal, 2010: Influence of tropical convection on the Southern Hemisphere ozone maximum during the winter to spring transition. *J. Geophys. Res.*, **115**, D14118, https://doi.org/10.1029/2009JD012883.

Hoerling, M. P., A. Kumar, and M. Zhong, 1997: El Niño, La Niña, and the nonlinearity of their teleconnections. *J. Climate*, **10**, 1769–1786, https://doi.org/10.1175/1520-0442(1997)010<1769:ENOLNA>2.0.CO;2.

Hoskins, B. J., I. N. James, and G. H. White, 1983: The shape, propagation and mean-flow interaction of large-scale weather systems. *J. Atmos. Sci.*, **40**, 1595–1612, https://doi.org/10.1175/1520-0469(1983)040<1595:TSPAMF>2.0.CO;2.

Hu, K., S.-P. Xie, and G. Huang, 2017: Orographically anchored El Niño effect on summer rainfall in central China. *J. Climate*, **30**, 10 037–10 045, https://doi.org/10.1175/JCLI-D-17-0312.1.

——, G. Huang, S.-P. Xie, and S.-M. Long, 2019: Effect of the mean flow on the anomalous anticyclone over the Indo-northwest Pacific in post–El Niño summers. *Climate Dyn.*, **53**, 5725–5741, https://doi.org/10.1007/s00382-019-04893-z.

Ji, X., J. D. Neelin, and C. R. Mechoso, 2016: Baroclinic-to-barotropic pathway in El Niño–Southern Oscillation teleconnections from the viewpoint of a barotropic Rossby wave source. *J. Atmos. Sci.*, **73**, 4989–5002, https://doi.org/10.1175/JAS-D-16-0053.1.

Jiang, W., G. Huang, K. Hu, R. Wu, H. Gong, X. Chen, and W. Tao, 2017: Diverse relationship between ENSO and northwest Pacific summer climate among CMIP5 models: Dependence on the ENSO decay pace. *J. Climate*, **30**, 109–127, https://doi.org/10.1175/JCLI-D-16-0365.1.

Jin, D., and B. P. Kirtman, 2009: Why the Southern Hemisphere ENSO responses lead ENSO. *J. Geophys. Res.*, **114**, D23101, https://doi.org/10.1029/2009JD012657.

Johnson, N. C., and Y. Kosaka, 2016: The impact of eastern equatorial Pacific convection on the diversity of boreal winter El Niño teleconnection patterns. *Climate Dyn.*, **47**, 3737–3765, https://doi.org/10.1007/s00382-016-3039-1.

Kanamitsu, M., W. Ebisuzaki, J. Woollen, S.-K. Yang, J. J. Hnilo, M. Fiorino, and G. L. Potter, 2002: NCEP–DOE AMIP-II reanalysis (R-2). *Bull. Amer. Meteor. Soc.*, **83**, 1631–1644, https://doi.org/10.1175/BAMS-83-11-1631.

Karoly, D. J., 1989: Southern Hemisphere circulation features associated with El Niño–Southern Oscillation events. *J. Climate*, **2**, 1239–1252, https://doi.org/10.1175/1520-0442(1989)002<1239:SHCFAW>2.0.CO;2.

Kim, M., C. Yoo, M.-K. Sung, and S. Lee, 2020: Classification of wintertime atmospheric teleconnection patterns in the Northern Hemisphere. *J. Climate*, **34**, 1847–1861, https://doi.org/10.1175/JCLI-D-20-0339.1.

Kosaka, Y., and H. Nakamura, 2006: Structure and dynamics of the summertime Pacific–Japan teleconnection pattern. *Quart. J. Roy. Meteor. Soc.*, **132**, 2009–2030, https://doi.org/10.1256/qj.05.204.

Lau, N. C., A. Leetmaa, M. J. Nath, and H. L. Wang, 2005: Influences of ENSO-induced Indo–western Pacific SST anomalies on extratropical atmospheric variability during the boreal summer. *J. Climate*, **18**, 2922–2942, https://doi.org/10.1175/JCLI3445.1.

L'Heureux, M. L., and D. W. J. Thompson, 2006: Observed relationships between the El Niño–Southern Oscillation and the extratropical zonal-mean circulation. *J. Climate*, **19**, 276–287, https://doi.org/10.1175/JCLI3617.1.

Li, X., D. M. Holland, E. P. Gerber, and C. Yoo, 2014: Impacts of the north and tropical Atlantic Ocean on the Antarctic Peninsula and sea ice. *Nature*, **505**, 538–542, https://doi.org/10.1038/nature12945.

——, ——, ——, and ——, 2015: Rossby waves mediate impacts of tropical oceans on West Antarctic atmospheric circulation in austral winter. *J. Climate*, **28**, 8151–8164, https://doi.org/10.1175/JCLI-D-15-0113.1.

Liu, B., G. Huang, K. Hu, R. Wu, H. Gong, P. Wang, and G. Zhao, 2018: The multidecadal variations of the interannual relationship between the East Asian summer monsoon and ENSO in a coupled model. *Climate Dyn.*, **51**, 1671–1686, https://doi.org/10.1007/s00382-017-3976-3.

Liu, L., and Coauthors, 2019: Dominant interannual covariations of the East Asian–Australian land precipitation during boreal winter. *J. Climate*, **32**, 3279–3296, https://doi.org/10.1175/JCLI-D-18-0477.1.

Liu, Z., and M. Alexander, 2007: Atmospheric bridge, oceanic tunnel, and global climatic teleconnections. *Rev. Geophys.*, **45**, RG2005, https://doi.org/10.1029/2005RG000172.

Lu, J., G. Chen, and D. M. W. Frierson, 2008: Response of the zonal mean atmospheric circulation to El Niño versus global warming. *J. Climate*, **21**, 5835–5851, https://doi.org/10.1175/2008JCLI2200.1.

Mo, K. C., and R. W. Higgins, 1998: The Pacific–South American modes and tropical convection during the Southern Hemisphere winter. *Mon. Wea. Rev.*, **126**, 1581–1596, https://doi.org/10.1175/1520-0493(1998)126<1581:TPSAMA>2.0.CO;2.

——, and J. N. Paegle, 2001: The Pacific–South American modes and their downstream effects. *Int. J. Climatol.*, **21**, 1211–1229, https://doi.org/10.1002/joc.685.

Mo, R., J. Fyfe, and J. Derome, 1998: Phase-locked and asymmetric correlations of the wintertime atmospheric patterns with the ENSO. *Atmos.–Ocean*, **36**, 213–239, https://doi.org/10.1080/07055900.1998.9649612.

Poli, P., and Coauthors, 2016: ERA-20C: An atmospheric reanalysis of the twentieth century. *J. Climate*, **29**, 4083–4097, https://doi.org/10.1175/JCLI-D-15-0556.1.

Rayner, N. A., D. E. Parker, E. B. Horton, C. K. Folland, L. V. Alexander, D. P. Rowell, E. C. Kent, and A. Kaplan, 2003: Global analyses of sea surface temperature, sea ice, and night marine air temperature since the late nineteenth century. *J. Geophys. Res.*, **108**, 4407, https://doi.org/10.1029/2002JD002670.

Rind, D., M. Chandler, J. Lerner, D. G. Martinson, and X. Yuan, 2001: Climate response to basin-specific changes in latitudinal temperature gradients and implications for sea ice variability. *J. Geophys. Res.*, **106**, 20 161–20 173, https://doi.org/10.1029/2000JD900643.

Robinson, W. A., 2002: On the midlatitude thermal response to tropical warmth. *Geophys. Res. Lett.*, **29**, 1190–4066, https://doi.org/10.1029/2001GL014158.

Roeckner, E., and Coauthors, 2003: The atmospheric general circulation model ECHAM-5. Part I: Model description. Max-Planck Institute for Meteorology Rep. 349, http://hdl.handle.net/11858/00-001M-0000-0012-0144-5.

Schneider, D. P., Y. Okumura, and C. Deser, 2012: Observed Antarctic interannual climate variability and tropical linkages. *J. Climate*, **25**, 4048–4066, https://doi.org/10.1175/JCLI-D-11-00273.1.

Seager, R., N. Harnik, Y. Kushnir, W. Robinson, and J. Miller, 2003: Mechanisms of hemispherically symmetric climate variability. *J. Climate*, **16**, 2960–2978, https://doi.org/10.1175/1520-0442(2003)016<2960:MOHSCV>2.0.CO;2.

Simmons, A. J., J. M. Wallace, and G. W. Branstator, 1983: Barotropic wave propagation and instability, and atmospheric teleconnection patterns. *J. Atmos. Sci.*, **40**, 1363–1392, https://doi.org/10.1175/1520-0469(1983)040<1363:BWPAIA>2.0.CO;2.

Tao, W., G. Huang, K. Hu, X. Qu, G. Wen, and H. Gong, 2015: Interdecadal modulation of ENSO teleconnections to the Indian Ocean Basin Mode and their relationship under global warming in CMIP5 models. *Int. J. Climatol.*, **35**, 391–407, https://doi.org/10.1002/joc.3987.

——, ——, R. Wu, K. Hu, P. Wang, and H. Gong, 2018: Origins of biases in CMIP5 models simulating northwest Pacific summertime atmospheric circulation anomalies during the decaying phase of ENSO. *J. Climate*, **31**, 5707–5729, https://doi.org/10.1175/JCLI-D-17-0289.1.

Ting, M. F., and L. H. Yu, 1998: Steady response to tropical heating in wavy linear and nonlinear baroclinic models. *J. Atmos. Sci.*, **55**, 3565–3582, https://doi.org/10.1175/1520-0469(1998)055<3565:SRTTHI>2.0.CO;2.

Trascasa-Castro, P., A. C. Maycock, Y. Y. S. Yiu, and J. K. Fletcher, 2019: On the linearity of the stratospheric and Euro-Atlantic sector response to ENSO. *J. Climate*, **32**, 6607–6626, https://doi.org/10.1175/JCLI-D-18-0746.1.

Trenberth, K. E., G. W. Branstator, D. Karoly, A. Kumar, N. C. Lau, and C. Ropelewski, 1998: Progress during TOGA in understanding and modeling global teleconnections associated with tropical sea surface temperatures. *J. Geophys. Res.*, **103**, 14 291–14 324, https://doi.org/10.1029/97JC01444.

Wang, Y., G. Huang, and K. Hu, 2020: Internal variability in multidecadal trends of surface air temperature over Antarctica in austral winter in model simulations. *Climate Dyn.*, **55**, 2835–2847, https://doi.org/10.1007/s00382-020-05412-1.

Watanabe, M., and M. Kimoto, 2000: Atmosphere–ocean thermal coupling in the North Atlantic: A positive feedback. *Quart. J. Roy. Meteor. Soc.*, **126**, 3343–3369, https://doi.org/10.1002/qj.49712657017.

Wilson, A. B., D. H. Bromwich, K. M. Hines, and S.-H. Wang, 2014: El Niño flavors and their simulated impacts on atmospheric circulation in the high southern latitudes. *J. Climate*, **27**, 8934–8955, https://doi.org/10.1175/JCLI-D-14-00296.1.

——, ——, and ——, 2016: Simulating the mutual forcing of anomalous high southern latitude atmospheric circulation by El Niño flavors and the southern annular mode. *J. Climate*, **29**, 2291–2309, https://doi.org/10.1175/JCLI-D-15-0361.1.

Xie, S.-P., Y. Kosaka, Y. Du, K. Hu, J. S. Chowdary, and G. Huang, 2016: Indo-western Pacific Ocean capacitor and coherent climate anomalies in post-ENSO summer: A review. *Adv. Atmos. Sci.*, **33**, 411–432, https://doi.org/10.1007/s00376-015-5192-6.

Yang, S., and P. J. Webster, 1990: The effect of summer tropical heating on the location and intensity of the extratropical westerly jet streams. *J. Geophys. Res.*, **95**, 18 705–18 721, https://doi.org/10.1029/JD095iD11p18705.

Yiu, Y. Y. S., and A. C. Maycock, 2019: On the seasonality of the El Niño teleconnection to the Amundsen Sea region. *J. Climate*, **32**, 4829–4845, https://doi.org/10.1175/JCLI-D-18-0813.1.

Yuan, X., 2004: ENSO-related impacts on Antarctic sea ice: A synthesis of phenomenon and mechanisms. *Antarct. Sci.*, **16**, 415–425, https://doi.org/10.1017/S0954102004002238.

——, and D. G. Martinson, 2000: Antarctic sea ice extent variability and its global connectivity. *J. Climate*, **13**, 1697–1717, https://doi.org/10.1175/1520-0442(2000)013<1697:ASIEVA>2.0.CO;2.

Zhou, Z., S. Xie, X. Zheng, Q. Liu, and H. Wang, 2014: Global warming–induced changes in El Niño teleconnections over the North Pacific and North America. *J. Climate*, **27**, 9050–9064, https://doi.org/10.1175/JCLI-D-14-00254.1.